ACS OMEGA

http://pubs.acs.org/journal/acsodf

Article

Polythiophene (PTh)−TiO_2−Reduced Graphene Oxide (rGO) Nanocomposite Coating: Synthesis, Characterization, and Corrosion Protection Performance on Low-Carbon Steel in 3.5 wt % NaCl Solution

Mohammad Mobin* and Farina Ansar

Cite This: *ACS Omega* 2022, 7, 46717−46730

Read Online

ACCESS | Metrics & More | Article Recommendations

ABSTRACT: The ternary nanocomposite polythiophene (PTh)−TiO_2−reduced graphene oxide (rGO) (PTh-TiO_2-rGO) was synthesized by chemical oxidative polymerization with $FeCl_3$ used as the oxidizing agent. Fourier transform infrared (FTIR) spectroscopy, X-ray diffraction (XRD), Raman spectroscopy, scanning electron microscopy (SEM), and transmission electron microscopy (TEM) were used to characterize the synthesized nanocomposite, followed by its casting on a low-carbon steel (LCS) substrate using *N*-methyl-2-pyrrolidone (NMP) as a solvent and an epoxy resin and triethyl tetraamine as a binder and curing agent, respectively. Anticorrosion properties of the PTh-TiO_2-rGO nanocomposite in 3.5 wt % NaCl solution were established using open-circuit potential (OCP), electrochemical impedance spectroscopy (EIS), potentiodynamic polarization (PDP), salt spray test, immersion test, contact angle (CA) measurements, water uptake test, and SEM. Additionally, PTh and PTh-TiO_2 were separately synthesized, characterized, and subjected to anticorrosion tests following identical synthesis routes for comparison purposes. The results of the investigations demonstrated that the PTh-TiO_2-rGO nanocomposite coating provides superior protection in 3.5 wt % NaCl solution compared to pure PTh and PTh-TiO_2 coatings, which are evident from its lowest corrosion current density (I_{corr}) (0.570×10^{-6} A cm^{-2}), highest positive shift in corrosion potential (E_{corr}) (−0.578 V), highest impedance and phase angle (3.56×10^3 Ω cm^2 and 70°, respectively), highest hydrophobicity (CA 94°), and highest protection efficiency (99%). These results show that the proposed nanocomposite coating provides better corrosion protection in a 3.5 wt % NaCl solution than other coatings.

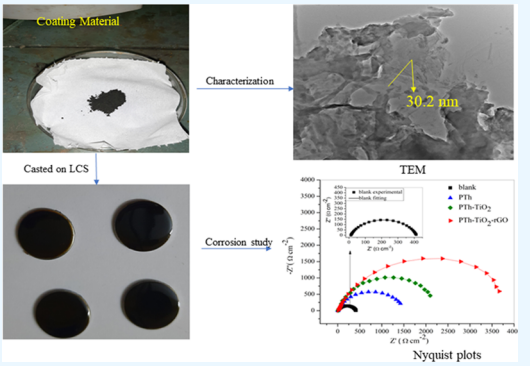

INTRODUCTION

Metal corrosion has had a significant impact on the global economy in the modern industrial period. Corrosion of the metallic surface or its inside occurs due to oxidation and reduction reactions occurring in the presence of salt and water.[1] Globally, the annual cost of corrosion is estimated to be roughly 3.5 wt % of the gross domestic product (GDP). Therefore, corrosion protection is a highly crucial factor in the metallurgical industry. One of the most effective strategies for protecting metals against corrosion has been the use of protective coatings. Chromate-based coatings are a well-known and extremely effective anticorrosive agent, but their carcinogenic nature makes them particularly dangerous to people's health.

Conducting polymers (CPs)-based coatings on metal surfaces have been exploited to protect metals against corrosion.[2] Because of their remarkable anticorrosion capacity and ecofriendliness, CPs are gaining popularity as either film-forming corrosive inhibitors or protective coatings.[3] CPs have gained a lot of interest among these coatings because of their unique qualities such as environmental stability, tuneable high conductivity, and ease of fabrication.[4] CPs, such as polythiophene (PTh), have unique qualities such as strong environmental resilience, good electrical conductivity, and other special properties that make them a good candidate for the synthesis of protective coating material. However, several problems have arisen during the application of conducting polymer-based coatings.[5] CPs systems have efficient corrosion protection when they are in the conducting form (oxidized and doped states), whereas they lose the protection in their reduced form of films.[6,7] Furthermore, during redox reactions,

Received: September 2, 2022
Accepted: November 23, 2022
Published: December 8, 2022

the charge in the material surface is irreversibly lost, and the coating's protection efficacy reduces with time.[8] Additionally, CPs coatings generally have a porous nature; they bind to metal surfaces weakly. Furthermore, due to the ion-exchange capability of the polymer, the protective efficacy of the coating may be decreased when the CPs layer is exposed to local corrosion caused by small and aggressive anions. As a result, there has been an emerging interest in composite/nanocomposite coatings made from CPs with various metal oxides to overcome the CPs' shortcomings. The resultant composites/nanocomposites have shown superior mechanical and physicochemical performances, as well as improved barrier and adhesion properties.[9,10] The corrosion resistance of various coatings has been studied in the presence of several nanoparticles (NPs), including TiO_2, ZnO, MgO, Fe_2O_3, ZrO_2, and Cr_2O_3.[11−17] Titanium dioxide (TiO_2) has been widely used as a pigment in paints. It was regarded worthwhile to use nanoparticles TiO_2 as a metal oxide additive in the composites because it could improve dispersion as well as barrier performance of the coatings.[18] Reduced graphene oxide (rGO) is a two-dimensional (2D) nanosheet made up of sp^2-hybridized carbon atoms that have attracted the attention of researchers due to its high conductivity, stability, high transmittance, and excellent mechanical properties. It is distinguished by high specific surface area and weak van der Waals interactions between adjacent layers. rGO, as a two-dimensional carbon material, is the thinnest anticorrosive material.[19] rGO's other unique properties, including chemical inertness, outstanding thermal and electrical conductivity, amazing flexibility, and molecular permeability, make it also a promising anticorrosion material.[20−23]

Keeping the above-mentioned facts in mind, the present work was envisaged and a polythiophene-based nanocomposite containing TiO_2 NPs and rGO was synthesized and characterized using Fourier transform infrared (FTIR) spectroscopy, Raman spectroscopy, X-ray diffraction (XRD), scanning electron microscopy (SEM), and transmission electron microscopy (TEM). The polythiophene−TiO_2−rGO nanocomposite was cast on LCS substrate and their anticorrosion properties in 3.5 wt % NaCl solutions were investigated using open-circuit potential (OCP), potentiodynamic polarization (PDP), electrochemical impedance spectroscopy (EIS), contact angle, water uptake, immersion test, and most accelerated salt spray test. Polythiophene and polythiophene−TiO_2 nanocomposite were separately synthesized, characterized, and investigated for their anticorrosion characteristics for comparison purposes.

RESULTS AND DISCUSSION

FTIR Study. The FTIR spectra of PTh, PTh-TiO_2, and PTh-TiO_2-rGO nanocomposites are given in Figure 1. A wide absorption band at 3400 cm^{-1} is identified in the PTh spectrum, as shown in Figure 1a, which may be related to the O−H stretching vibration. The peak at 1625 cm^{-1} is due to the C=C stretching mode of vibration, whereas the peak at 1469 cm^{-1} is due to the C−C mode of vibration. The peaks at 2920 and 2852 cm^{-1} are corresponding to the stretching vibrations of the C−H bond. The absorption band at 1114 cm^{-1} is due to the C−H bending vibration out of the plane of the PTh ring. The peak at 686 cm^{-1} is attributed to the C−S bending of the thiophene ring. The peak at 464 cm^{-1} can be assigned to the C−S−C ring mode of deformation.[24] In the spectrum of PTh-TiO_2 shown in Figure 1b, the peak at 689 cm^{-1} suggests C−S

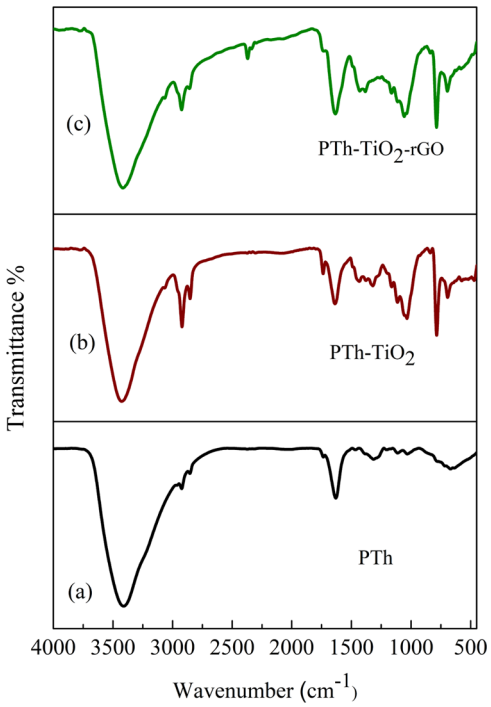

Figure 1. FTIR spectra of (a) PTh, (b) PTh-TiO_2, and (c) PTh-TiO_2-rGO nanocomposite.

in the thiophene ring.[25,26] The peak at 1041 cm^{-1} is due to the C−H bending aromatic vibration of PTh. The broad band at 3422 cm^{-1} corresponds to the O−H vibration. The peaks at 2920 and 2846 cm^{-1} correspond to the stretching vibrations of the C−H bond. The peaks at 1648 and 1737 cm^{-1} are due to the C=C stretching mode of vibration. The peaks at 1441 cm^{-1} are due to the C−C mode of vibration. The bands that appear at 400−750 cm^{-1} are responsible for stretching in the Ti−O−Ti vibration, suggesting the occurrence of TiO_2 in PTh-TiO_2. Figure 1c shows the spectrum of the PTh-TiO_2-rGO nanocomposite, which revealed almost identical peaks as that of the PTh-TiO_2 spectrum with only one extra peak appearing at 2371 cm^{-1}; this is attributed to graphene, suggesting the existence of graphene in the PTh-TiO_2-rGO nanocomposite. The functional groups and their corresponding wavenumber are given in Table 1.

XRD Analysis. Figure 2 depicts X-ray diffraction (XRD) patterns of PTh, TiO_2 NPs, PTh-TiO_2, and PTh-TiO_2-rGO nanocomposite. In the case of PTh (Figure 2a), a wide diffraction peak was observed within the region of 2θ = 20−30°, identifying the amorphous nature of polythiophene (PTh). Figure 2b shows the XRD pattern of pure TiO_2 NPs; the six main peaks are observed at 2θ = 27.94, 32.39, 37.80, 45.29, 47.91, and 57.26°, respectively, in accordance with the standard data (JCPDS No: 21-1272) and match with the crystal lattice planes 101, 004, 200, 105, 211, and 204, respectively.[27] The XRD pattern of PTh-TiO_2 (Figure 2c) shows five main peaks in addition to PTh characteristic broad peaks (at 2θ = 20−30°), which are detected at 2θ = 28.41, 32.28, 33.57, 38.02, and 47.87°, respectively, due to the presence of TiO_2 nanoparticles in the PTh-TiO_2. As shown in Figure 2d, the XRD pattern of the PTh-TiO_2-rGO nanocomposite is identical to that of the PTh-TiO_2, with one additional peak observed at 2θ = 70.16°, possibly due to PTh interaction with TiO_2 incorporated on graphene sheets.

https://doi.org/10.1021/acsomega.2c05678
ACS Omega 2022, 7, 46717−46730

Table 1. FTIR Vibrations Functional Groups

band (cm^{-1})	PTh	band (cm^{-1})	PTh-TiO_2	band (cm^{-1})	PTh-TiO_2-rGO
464	−C−S−C	400−750	−Ti−O−Ti	657	−Ti−O−Ti
686	−C−S	689	−C−S	782	−C−S
1114	−C−H (bending)	1041	−C−H (bending)	1045	−C−H (bending)
1469	−C−C	1441	−C−C	1405	−C−C
1625	−C═C	1648	−C═C (stretching)	1642	−C═C (stretching)
2800−2990	−C−H (stretching)	2846	−C−H (stretching)	2350	rGO
3400	−O−H	3422	−O−H	3418	−O−H

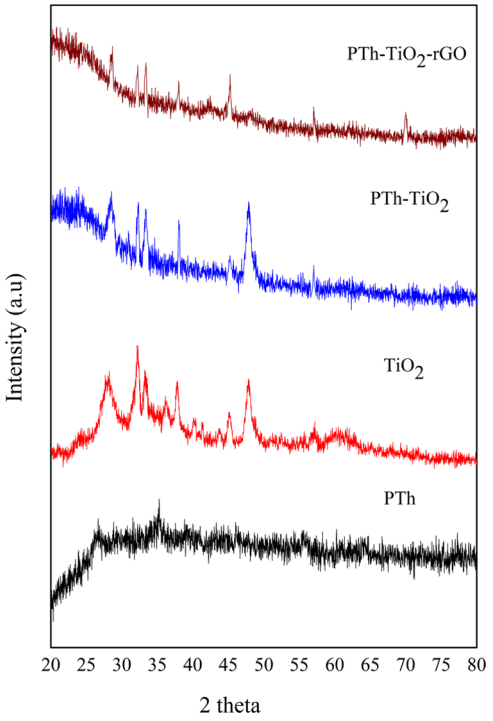

Figure 2. XRD patterns of PTh, TiO_2, PTh-TiO_2, and PTh-TiO_2-rGO nanocomposite.

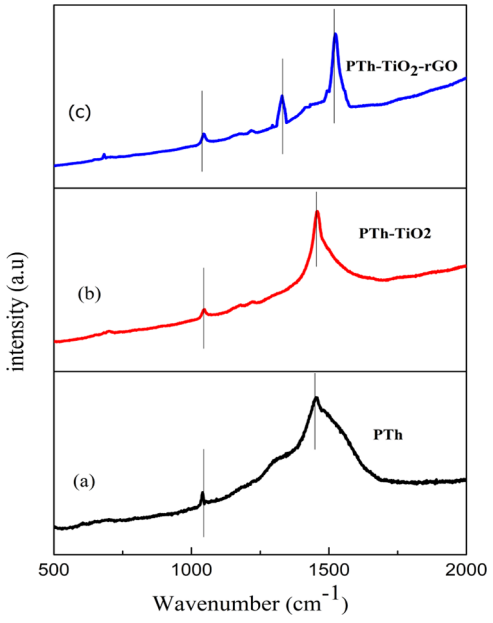

Figure 3. Raman spectra of (a) PTh, (b) PTh-TiO_2, and (c) PTh-TiO_2-rGO nanocomposite.

Raman Study. Figure 3 shows the Raman spectra of PTh, PTh-TiO_2, and PTh-TiO_2-rGO nanocomposite. The Raman spectrum of PTh (Figure 3a) reveals two significant peaks, with the first prominent peak at 1455 cm^{-1} corresponding to C═C stretching and the other small peak at 1038 cm^{-1} corresponding to C−C stretching with a C−H wagging component.[28] The characteristic peaks of PTh at 1038 and 1455 cm^{-1} shifted to 1050 and 1461 cm^{-1} in the case of PTh-TiO_2 (Figure 3b), whereas in the case of the PTh-TiO_2-rGO nanocomposite (Figure 3c), these peaks are witnessed at 1044 and 1523 cm^{-1}, and one additional peak is also found at 1326 cm^{-1}. A binding interaction between PTh and graphene nanosheets, which facilitates charge transfer from PTh to graphene nanosheets and interaction between PTh and graphene nanosheets, may be responsible for the significant change in the PTh characteristic peaks in PTh-TiO_2-rGO. The disruption of the symmetric hexagonal graphitic lattice is responsible for the D band of rGO, which is located at 1326 cm^{-1}, while the symmetric sp^2 C−C bonds in-plane stretching is responsible for the G band, which is located at 1523 cm^{-1}.

SEM/Energy-Dispersive X-ray Analysis (EDAX), and TEM Studies. Figure 4 depicts the SEM micrographs along with EDAX profiles of PTh, PTh-TiO_2, and PTh-TiO_2-rGO nanocomposite at different magnifications. The SEM images often indicate a flaky morphology, as shown in Figure 4a,b. In the case of PTh-TiO_2, the absence of free TiO_2 nanoparticles in the micrograph might be attributed to the TiO_2 nanoparticles' complete incorporation into the PTh matrix. The PTh-TiO_2 morphology exhibited a flaky or thin sheet-like structure interconnected with one another, resulting in a highly porous surface, as shown in Figure 4d,e. The change in morphology indicated that PTh and TiO_2 might have some interactions between TiO_2 and PTh. The porous nature of the material and its huge surface area play an important role in this study. Figure 4g,h shows the morphology of the PTh-TiO_2-rGO nanocomposite, which appears to be very different from pure PTh and PTh-TiO_2 due to the excellent interfacial wrapping of PTh-TiO_2 over graphene nanosheets. PTh-TiO_2 is well distributed on graphene nanosheets, resulting in flaky as well as sheet-like morphology. Because no loose graphene nanosheets are detected in the PTh-TiO_2-rGO nanocomposite, it is possible to conclude that PTh-TiO_2 successfully covers graphene nanosheets. Figure 4c,f,i depicts the EDAX profile of PTh, PTh-TiO_2, and PTh-TiO_2-rGO nanocomposite, respectively. The presence of elements C, S, Cl, and Fe in PTh (Figure 4c); C, S, Ti, O, and Fe in PTh-TiO_2 (Figure 4f); and C, S, Ti, O, Cl, and Fe in the PTh-TiO_2-rGO nanocomposite (Figure 4i) are evident from the EDAX profiles.

Figure 5 shows TEM images of PTh, PTh-TiO_2, and PTh-TiO_2-rGO nanocomposite. In the case of PTh, the presence of nanorods and flaky microstructure can be revealed in Figure 5a, which is also in SEM images. The TiO_2 nanoparticles

https://doi.org/10.1021/acsomega.2c05678
ACS Omega 2022, 7, 46717−46730

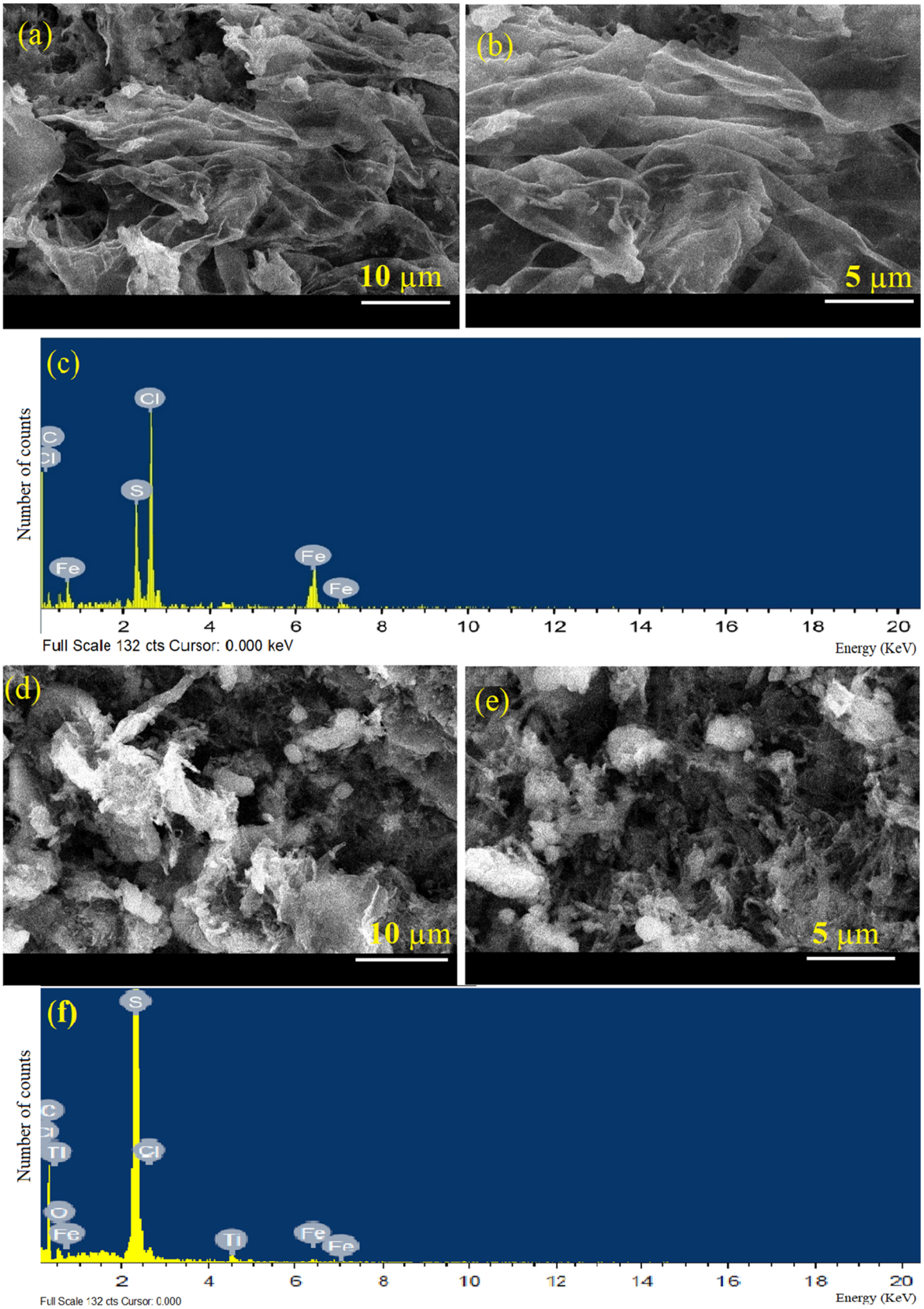

Figure 4. continued

https://doi.org/10.1021/acsomega.2c05678
ACS Omega 2022, 7, 46717−46730

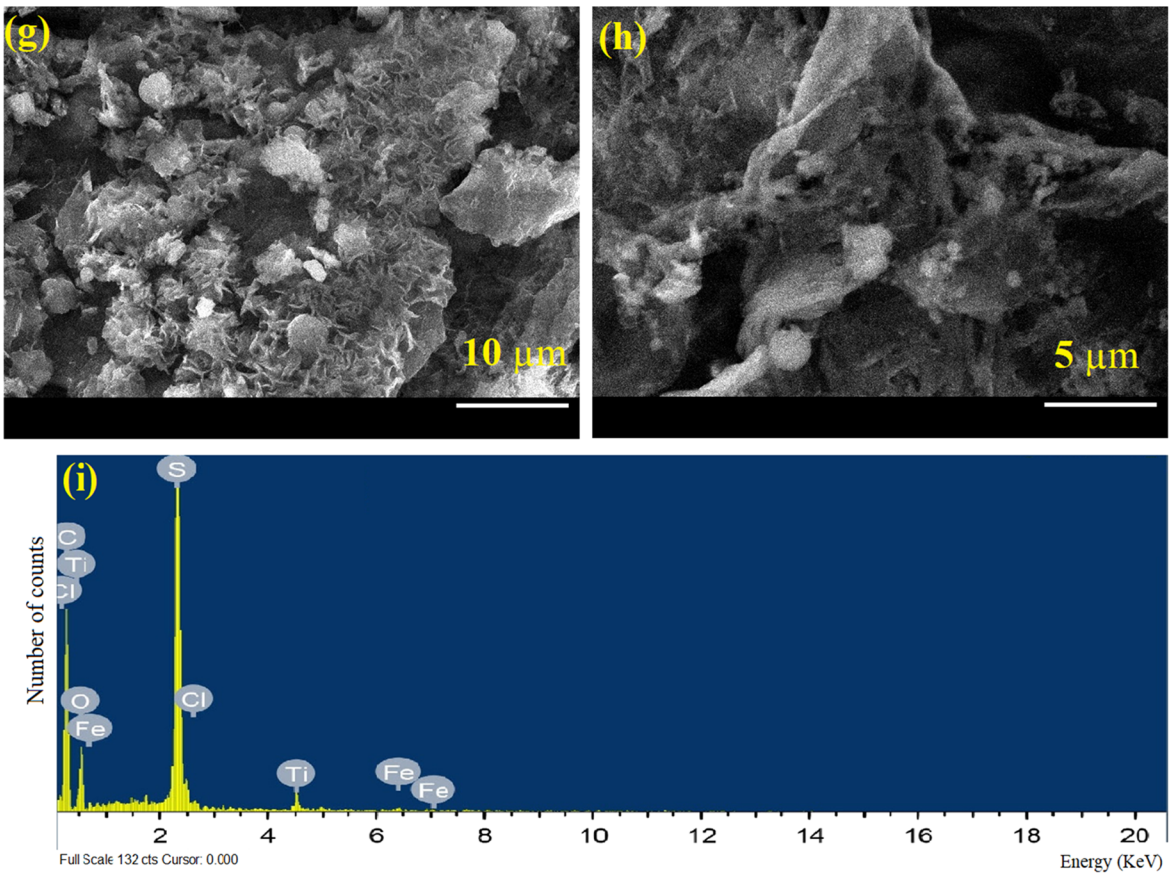

Figure 4. SEM micrographs of (a, b) PTh, (d, e) PTh-TiO_2, and (g, h) PTh-TiO_2-rGO nanocomposite at different magnifications, and (c, f, and i) the EDAX spectra prove the elemental composition of synthesized compounds.

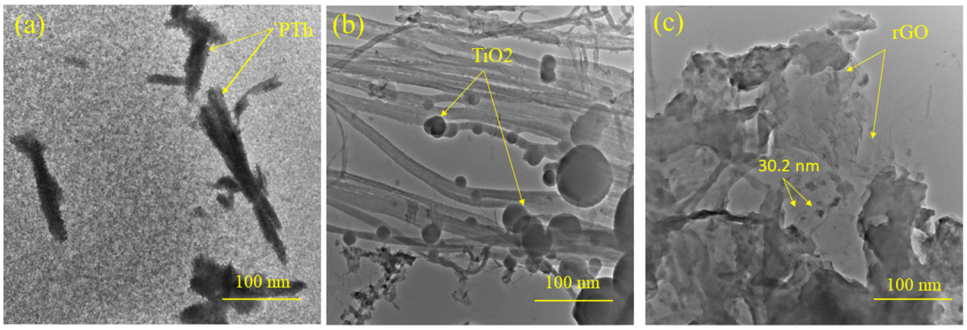

Figure 5. TEM images of (a) PTh, (b) PTh-TiO_2, and (c) PTh-TiO_2-rGO nanocomposite at a magnification of 100 nm.

(dark-colored) are enclosed within the gray background of the PTh matrix, as shown in the TEM image of the PTh-TiO_2 nanocomposite (Figure 5b). The existence of a strong electrostatic interaction between the sulfur atom of PTh and the TiO_2 atoms, as illustrated in the TEM micrograph, may clarify the complete deposition of PTh on TiO_2 nanoparticles. The TiO_2 nanoparticles were absorbed on graphene (rGO) sheets upon which PTh nanorods were deposited (Figure 5c), indicating that TiO_2 nanoparticles were successfully incorporated into rGO sheets for a nanocomposite containing PTh nanorods.

CORROSION STUDIES

OCP. The OCP change (potential vs time) graphs for blank steel, PTh, PTh-TiO_2, and PTh-TiO_2-rGO nanocomposite-deposited LCS coupons in 3.5 wt % NaCl solution at 40 °C temperature for an 11,000 s immersion duration is shown in Figure 6. These curves demonstrated that the time was sufficient to achieve steady-state potential. The PTh, PTh-TiO_2, and PTh-TiO_2-rGO nanocomposite coatings produce a positive (noble) shift in OCP when compared to blank, with the maximum positive (noble) shift occurring in the case of the PTh-TiO_2-rGO nanocomposite coating. This indicates the highest level of protection provided by the PTh-TiO_2-rGO nanocomposite coating. The order of positive shift in OCP of coated steel is as follows: PTh-TiO_2-rGO > PTh-TiO_2 > PTh. The more positive shift in the values of OCP indicates their high corrosion resistance, which is a result of both barrier existence and the passive oxide layer effect at the coating interface.[29−31] The presence of rGO and TiO_2 in the PTh-TiO_2-rGO nanocomposite coating has shifted the potential in a more noble direction and improved the coating's redox

https://doi.org/10.1021/acsomega.2c05678
ACS Omega 2022, 7, 46717−46730

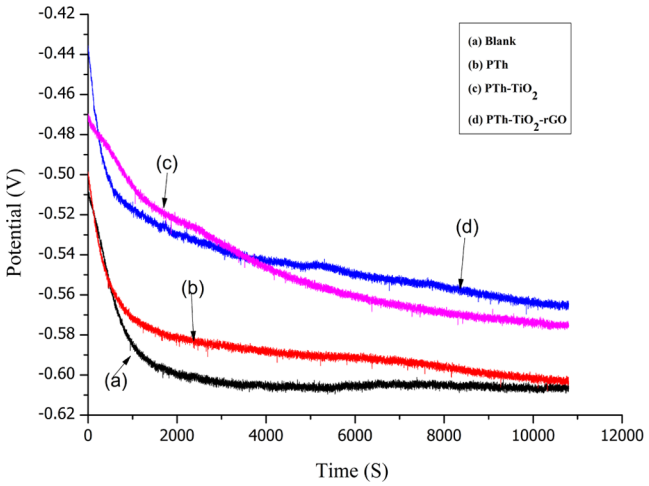

Figure 6. OCP variation for (a) blank, (b) PTh, (c) PTh-TiO_2, and (d) PTh-TiO_2-rGO nanocomposite during 11,000 s immersions in 3.5 wt % NaCl.

behavior and barrier characteristics.[32] The higher corrosion protection ability of the PTh-TiO_2-rGO and PTh-TiO_2 nanocomposite coatings over PTh for the full immersion time is due to a superior barrier effect, i.e., changes caused by the formation of a more adhesive, dense, and uniform layer on the steel surface. In the beginning, corrosion ions penetrate the coatings and reach the steel surface, resulting in the anodic dissolution of metal and a drop in the potential. Later on, the OCP levels stabilize due to the formation of a passive oxide layer on the coating/steel surface.

EIS Study. EIS is a nondestructive electrochemical approach used to determine the corrosion resistance of coatings. Impedance measurements were performed by immersing the test samples in a 3.5 wt % NaCl solution at room temperature. The impedance plots for blank and coated LCS specimens are shown as Nyquist and Bode plots (Figures 7–9). In Figure 7, the depressed semicircle, possibly due to surface heterogeneity or the presence of corrosion product, is depicted by nyquist curves. The diameter of the semicircle increases in the following order: PTh-TiO_2-rGO nanocomposite > PTh-TiO_2 > PTh. This is indicative of the higher protection ability of the PTh-TiO_2-rGO nanocomposite coating than that of PTh-TiO_2 and PTh coatings. The blank LCS impedance curve was fitted by an electrical equivalent circuit (Figure 8a), which comprises Rs (solution resistance),

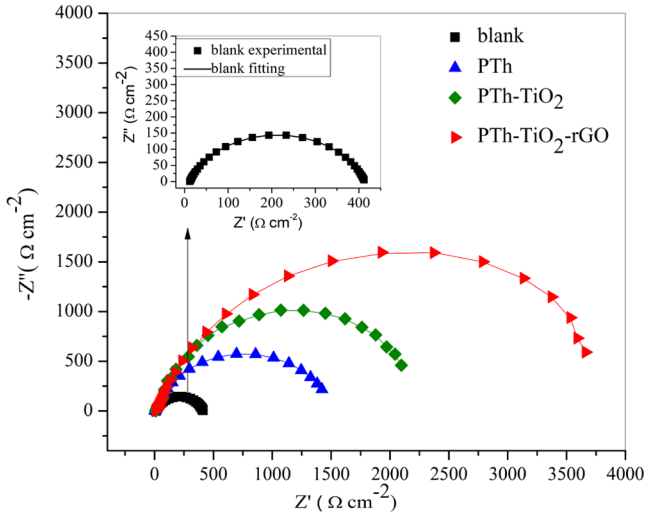

Figure 7. Nyquist plots in 3.5 wt % NaCl solution for blank, PTh, PTh-TiO_2, and PTh-TiO_2-rGO coated on LCS.

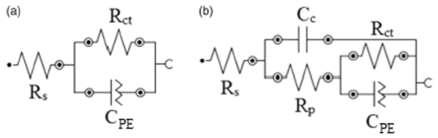

Figure 8. (a, b) Equivalent electrical circuits of (a) blank and (b) the coated LCS sample in 3.5 wt % NaCl.

CPE (double-layer capacitance), and R_{ct} (charge-transfer resistance). Impedance plots for coated LCS are fitted using an electrical equivalent circuit (Figure 8b), which includes R_s, C_c (coating capacitance), R_{ct}, and CPE. Instead of capacitance (C_{dl}), the constant phase element (CPE) is utilized to define the system's inhomogeneity. This element demonstrates the deviation from the genuine capacitance performance. The CPE's impedance can be calculated using eq 1

$$Z_{CPE} = Y_0^{-1}(j\omega)^{-n} \quad (1)$$

where Y_0 is the CPE constant, $j^2 = -1$ is an imaginary number, ω is the angular frequency in rad s^{-1} ($\omega = 2\pi f$, where f is the AC frequency in (Hz)), and n is the CPE exponent. If $n = 1$, the impedance of CPE is identical to that of a capacitor, and in this case, Y_0 gives a pure capacitance (C).[33] The following eq 2 is used to convert the impedance value of Y_0 to C_c.[34]

$$C_c = Y_0(\omega_{max})^{n-1} \quad (2)$$

where C_c is the coating capacitance and $\omega_{max} = 2\pi fm$ (where $2fm$ is the frequency at which the imaginary part of the impedance is at its maximum). The accuracy of the equivalent circuit was determined by the χ^2 values shown in Table 2. The lower the value of χ^2, the closeness of the circuit is the original phenomenon. Generally, the values of χ^2 between 10^{-3} and 10^{-5} are considered an ideal fit.[35]Table 2 shows the best-fit impedance parameters for blank and coated LCS. Usually, the parameter C_c exhibits the electrolytic solution diffusion into the coating. The barrier behavior and formation of a protective passive oxide layer on the LCS substrate are attributable to the increase in R_{ct} values. From Table 2, it can be seen that the PTh-TiO_2-rGO nanocomposite coating has the minimum C_c value and maximum value of R_{ct}, which implies that the PTh-TiO_2-rGO nanocomposite coating has maximum electrolyte penetration resistance and minimum electrolyte diffusion. In comparison to the PTh-TiO_2-rGO nanocomposite, the PTh-TiO_2 and pure PTh coatings have comparatively higher C_c and lower R_{ct} values, thus indicating that they provide less protection from electrolyte attack. Thus, the minimum C_c values combined with improved R_{ct} values for the PTh-TiO_2-rGO nanocomposite coating compared to the PTh-TiO_2 nanocomposite and pure PTh coatings give uncontested support for higher protection obtained by the PTh-TiO_2-rGO coating. The protection efficiency of different polymer coatings as evaluated from R_{ct} values is listed in Table 2. The better protection behavior of the PTh-TiO_2-rGO coating is due to the uniform dispersion of nanoparticles in the polymer matrix, which facilitated the formation of a homogeneous passive film on the LCS surface.

https://doi.org/10.1021/acsomega.2c05678
ACS Omega 2022, 7, 46717−46730

Table 2. Electrochemical Parameters Obtained for Uncoated and Coated LCS in 3.5 wt % NaCl Solution

				CPE			
sample	R_s(Ω cm^2)	R_{ct}(Ω cm^2)	C_c(F cm^{-2})	Y_0	n	χ^2	η%
blank	4.7228	404		1.91×10^{-3}	0.70496	0.37114	
PTh	108	1.8×10^3	7.0×10^{-6}	5.77×10^{-7}	1.2244	0.089362	77
PTh-TiO_2	3081	1.2×10^4	4.9×10^{-8}	1.30×10^{-5}	0.25989	0.06097	96.6
PTh-TiO_2-rGO	20,879	3.6×10^4	1.9×10^{-9}	5.44×10^{-7}	0.50874	0.089362	99.0

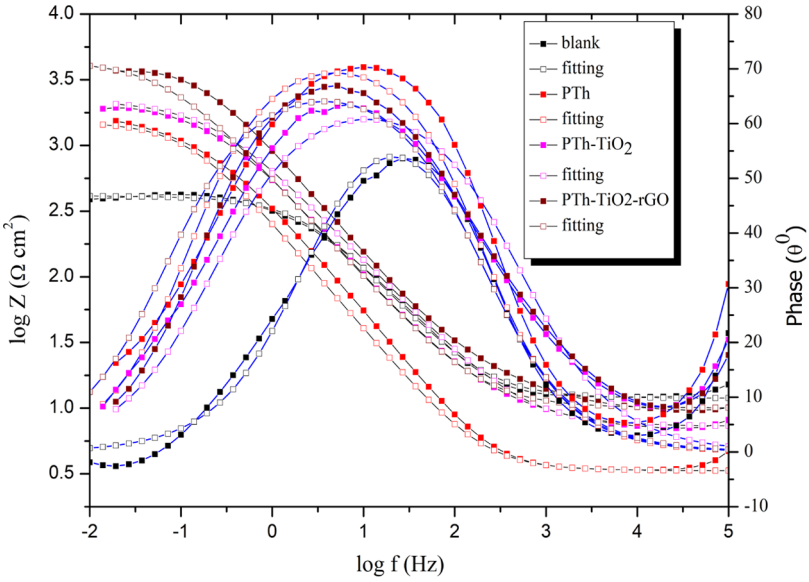

Figure 9. Bode plots (impedance and phase angle) for uncoated and coated LCS in 3.5 wt % NaCl.

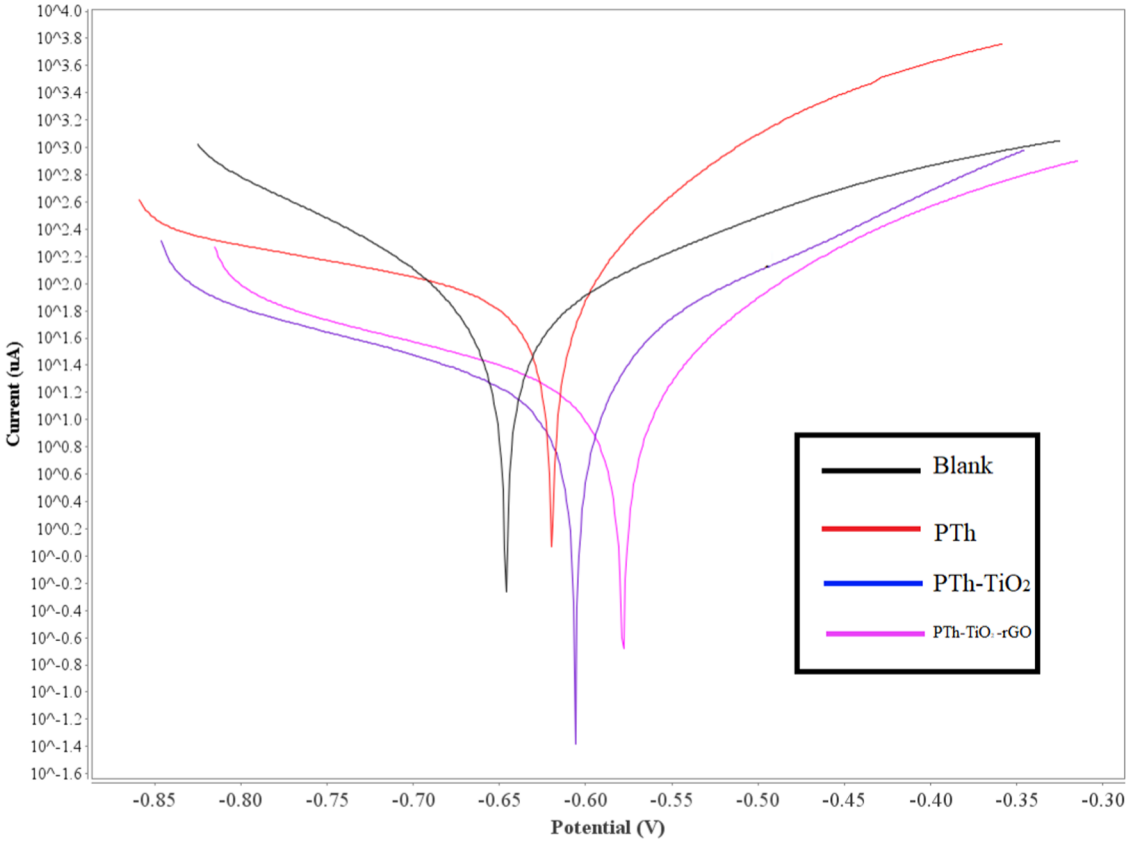

Figure 10. Tafel polarization curves for blank, PTh, PTh-TiO_2, and PTh-TiO_2-rGO nanocomposite-coated LCS in 3.5 wt % NaCl solution.

https://doi.org/10.1021/acsomega.2c05678
ACS Omega 2022, 7, 46717−46730

Table 3. Electrochemical Parameters for the Coated LCS Specimen Immersed in 3.5 wt % NaCl Solution Obtained from the Tafel Polarization Plot

sample	I_{corr}(A cm^{-2})	E_{corr} (V)	R_p(Ω cm^2)	b_a(V dec^{-1})	b_c(V dec^{-1})	*PE%*	*CR*(mm year^{-1})
blank	1.267×10^{-4}	−0.650	514	0.2199	0.3426		1.48968
PTh	3.478×10^{-5}	−0.620	949	0.5854	0.1022	72	0.6717
PTh-TiO_2	4.310×10^{-6}	−0.605	1754	1.33	0.19206	96	0.43026
PTh-TiO_2-rGO	0.570×10^{-6}	−0.578	2091	1.63299	0.2098	99	0.27622

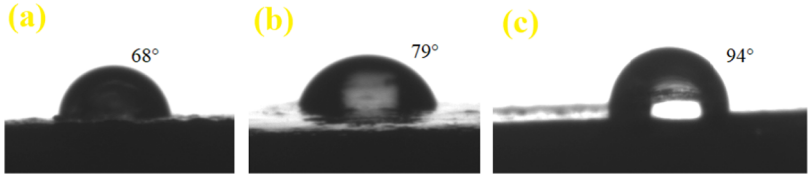

Figure 11. Contact angle images of polymeric coatings of (a) PTh, (b) PTh-TiO_2, and (c) PTh-TiO_2-rGO nanocomposite on LCS coupons.

The Bode plots (impedance and phase angle) are depicted in Figure 9, which further substantiates the superior corrosion protection performance of the PTh-TiO_2-rGO nanocomposite coating compared to that of PTh-TiO_2 and PTh coatings. It is evident from the Bode plots that with a change in frequency, a change in impedance and phase angle has taken place. The presence of the PTh-TiO_2-rGO nanocomposite coating on LCS has given rise to the highest increase in impedance value and more negative phase angle relative to PTh-TiO_2 and PTh coatings, thereby further establishing its superior corrosion protection ability in 3.5 wt % NaCl solution.

PDP Measurements. PDP analysis was used to determine the rate of corrosion and the nature of corrosion inhibition activity of coatings that protect the coated metal following anodic, cathodic, or mixed mechanisms (Figure 10). Tafel plots were utilized to measure electrochemical characteristics such as I_{corr}, E_{corr}, polarization resistance (R_p), anodic and cathodic Tafel slopes (b_a and b_c), corrosion rate (CR), and protection efficiency (η), as shown in Table 3. The E_{corr} value of samples coated with PTh, PTh-TiO_2, and PTh-TiO_2-rGO nanocomposite coatings shifted in the positive direction (anodic shift) as compared to the blank; the highest positive shift in the E_{corr} value was observed in case of the PTh-TiO_2-rGO nanocomposite coating, thus establishing its highly protective nature. The strong barrier property and highest corrosion resistance of the PTh-TiO_2-rGO nanocomposite coating were also established by its lowest I_{corr} (0.570×10^{-6} A cm^{-2}) and highest R_p (2091 Ω cm^2) values in comparison to PTh (3.478×10^{-5} A cm^{-2} and 949 Ω cm^2, respectively) and PTh-TiO_2 (4.310×10^{-6} A cm^{-2} and 1754 Ω cm^2, respectively) coatings. The protection efficiency (η) of the coatings was calculated from corrosion current density (I_{corr}) values as given in eq 3

$$\text{PE } \% = \frac{I^{\circ}_{corr} - I_{corr}}{I^{\circ}_{corr}} \times 100 \quad (3)$$

Here, I°_{corr} and I_{corr} present corrosion current densities for blank and coated samples, respectively. The PTh-TiO_2-rGO nanocomposite coating exhibited the highest protection efficiency of 99%. The results of PDP are consistent with EIS results.

Contact Angle. The images obtained by the sessile drop method for contact angle (CA) measurements are shown in Figure 11. This test is beneficial for determining the wettability of the coated surfaces where a low CA indicates the coating's wetting capacity. In this test, water is used as a test liquid to determine whether a surface is naturally hydrophilic or hydrophobic. Hydrophobic surfaces are regarded as anticorrosive due to their ability to repel water and so inhibit corrosion reactions.[36] The CA of pure PTh coating was observed to be 68° (Figure 11a), indicating that the coating surface is hydrophilic, having more wettability. However, in the case of the PTh-TiO_2 coating, dispersion of TiO_2 NPs in the PTh matrix elevates the CA to 79° (Figure 11b), thus indicating a decrease in wettability and an increase in hydrophobicity. The PTh-TiO_2-rGO nanocomposite coating having rGO achieved a CA of 94° (Figure 11c), showing that the rGO dispersion in the PTh-TiO_2 polymer coating had transformed it from hydrophilic to hydrophobic, making the nanocomposite coating more effective against corrosion protection by effectively reducing its wettability. Generally, the wettability of a coating is determined by its surface roughness and minimum surface energy. The incorporation of rGO in the PTh-TiO_2-rGO nanocomposite coating resulted in a reduced surface energy structure. This hydrophobic surface efficiently blocks the adsorption of corrodents, lowering the possibility of corrosive media entering the coating, and providing better protection against corrosion.[37]

Water Uptake Test/Swelling Studies. The water uptake (swelling behavior) of PTh, PTh-TiO_2, and PTh-TiO_2-rGO nanocomposite was tested by ASTM D570. The polymer-coated circular samples were collected and cleaned with tissue paper before being weighed before and after being immersed in a 200 mL beaker with 100 mL of water for 60 days at room temperature to determine their water absorption capacity. The water quantity absorbed by the coatings was calculated using the specified eq 4, and the results are reported in Table 4.

$$X_t\ (\%) = \frac{X_2 - X_1}{X_1} \times 100 \quad (4)$$

Here, X_t denotes the coating's total water content, and x_1 and x_2 denote the coating's weight before and after water

Table 4. Water Uptake (Swelling Studies) of PTh, PTh-TiO_2, and PTh-TiO_2-rGO Nanocomposite Coatings

s.no.	coating type	X_1 (g)	X_2 (g)	X_t, gain %
1	PTh	2.1288	2.2041	3.53
2	PTh-TiO_2	2.1778	2.2394	2.82
3	PTh-TiO_2-rGO	2.1939	2.2148	0.952

https://doi.org/10.1021/acsomega.2c05678
ACS Omega 2022, 7, 46717−46730

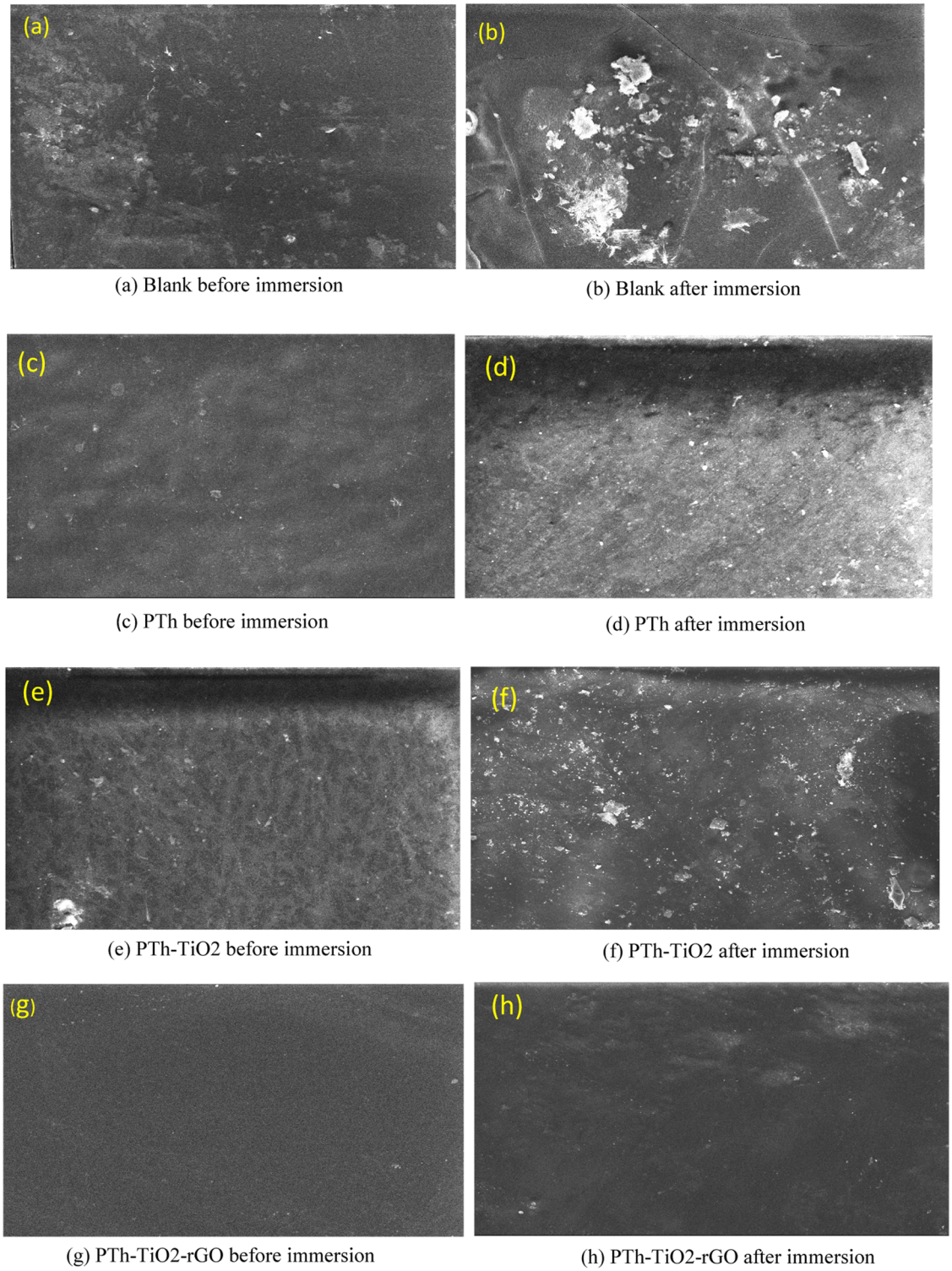

Figure 12. (a–h) SEM images of uncoated and coated steel surface before and after immersion test for 60 days in 3.5 wt % NaCl solution.

immersion, respectively. Table 4 shows that the PTh-TiO_2-rGO nanocomposite coating had the least change in weight before and after dipping for 60 days in water, indicating that no major swelling occurred in the PTh-TiO_2-rGO coating during the water uptake test.

Immersion Test of Coatings. The immersion test was performed in 3.5 wt % NaCl solution for 60 days on blank, PTh, PTh-TiO_2, and PTh-TiO_2-rGO nanocomposite coatings to investigate the permeability of corrosive ions through the coated surface on a qualitative level.[38] Before and after immersion, SEM was utilized to examine the morphology of these coatings (Figure 12). The blank surface after immersion in the electrolyte is badly corroded with many small pits, cracks, and salt accumulated on the surface, as seen in Figure 12b, whereas the PTh- and PTh-TiO_2-coated steel surfaces (Figure 12d,f, respectively) have some visible micropores and corrosion products. PTh-TiO_2-rGO nanocomposite-coated steel surface after exposure to the corrodent (Figure 12h),

https://doi.org/10.1021/acsomega.2c05678
ACS Omega 2022, 7, 46717−46730

Table 5. Comparison of the Protection Efficiency of the Present System with Other Systems Obtained for LCS in 3.5 wt % NaCl

s.no.	system	medium/metal used	% η	reference
1	PTh-TiO_2-rGO	3.5 wt % NaCl/LCS	99	present work
2	polyaniline/graphene	3.5 wt % NaCl/steel	53.49	39
3	Cu/PPy/TiO_2	3.5 wt % NaCl/Cu	72.8	40
4	PPy/TiO_2	0.5M H_2SO_4/steel	94.15	41
5	PANI-Fe_2O_3 composite	3.5 wt % NaCl/steel		42

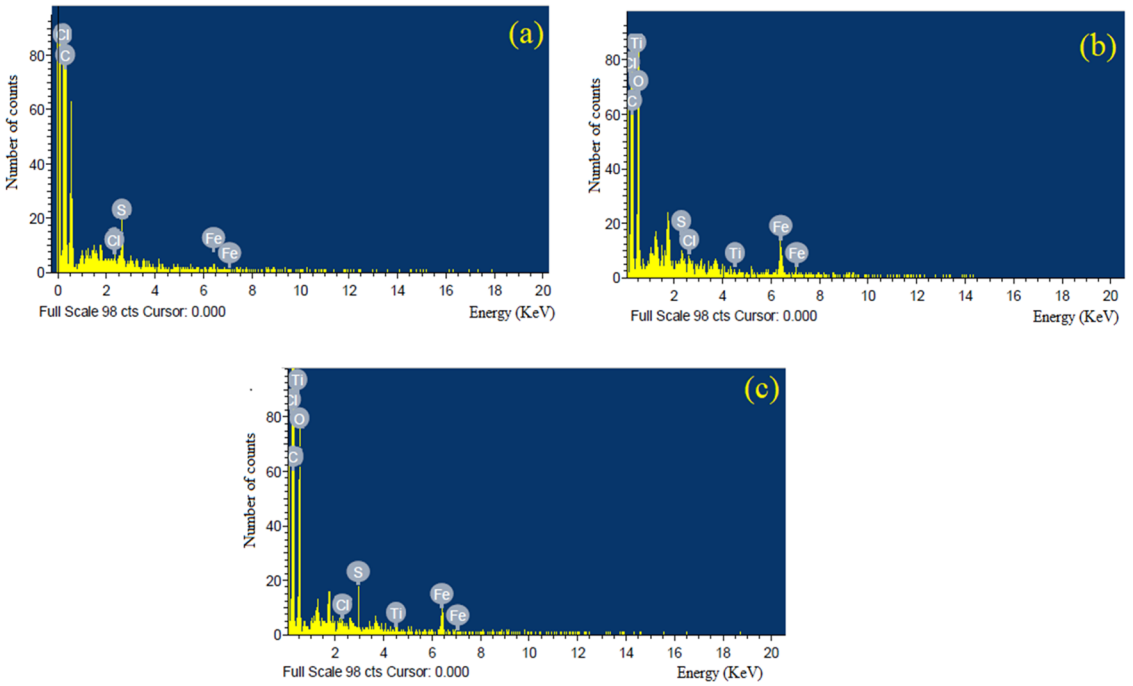

Figure 13. EDAX spectra of coatings cast on LCS: (a) PTh, (b) PTh-TiO_2, and (c) PTh-TiO_2-rGO nanocomposite after immersion in 3.5 wt % NaCl solution.

on the other hand, is still compact and dense, with minimal corrosion products on the surface. Even after long-term immersion in a 3.5 wt % NaCl solution, PTh-TiO_2-rGO nanocomposite coating exhibits good performance and provides superior protection against steel corrosion. Moreover as compared to previously studied conducting polymers based nanocomposite anticorrosive coatings PTh-TiO_2-rGO coating provided higher protection efficiency in Table 5.

EDAX Analysis of Coatings. Figure 13a−c depicts the EDAX spectra of PTh, PTh-TiO_2, and PTh-TiO_2-rGO nanocomposite coatings after their immersion in 3.5 wt % NaCl solution. The presence of identical elements in the coating materials before their casting and the casted coatings on LCS after immersion in corrosive solution is suggestive of the successful casting of coating materials on the LCS and no significant change in the coatings after their immersion in corrosive solution.

Salt Spray Test of Coatings. The barrier and adhesion capabilities of blank, PTh, PTh-TiO_2, and PTh-TiO_2-rGO nanocomposites coatings were further investigated using a salt spray test (as per ASTM designation B117) in a 5% NaCl solution at 90% humidity for various periods (0, 12, and 24 h).

The coated samples were scribed manually with a sharp blade and placed in a salt chamber that contained NaCl fumes that were continually sprayed on the samples while the chamber temperature was maintained at 35 ± 2 °C. The changes on the surface of the coatings were observed every 12 h. After 12 h, the test blank (uncoated sample) was fully corroded, as shown in Figure 14a. In the case of the PTh- and PTh-TiO_2 nanocomposite-coated sample, corrosion was observed on the scribed mark and associated with the penetration of corrosive ions into the coating matrix via scribe area and micropores, indicating the low barrier performance of coatings (Figure 14b,c). However, no discernible corrosion products were observed in the PTh-TiO_2-rGO nanocomposite coating even after a 24 h test, as shown in Figure 14d. The incorporation of rGO in the PTh-TiO_2-rGO nanocomposite coating increased significantly the coating's anticorrosion properties. Furthermore, graphene prevents steel oxidation in the scribed area according to these findings. These findings demonstrated that the incorporation of rGO in the PTh-TiO_2-rGO nanocomposite coating significantly improves the coating's anticorrosion performance.

Protective Mechanisms for Coatings. Corrosive media (water, O_2 molecules, and Cl ions) penetrate the coatings via defects and micropores, resulting in underneath metal corrosion. The presence of the PTh coating on the metal substrate not only serves as a barrier for corrosive media but may also participate in the reaction on the metal substrate resulting in the formation of complex passive oxides films, which may terminate the electron transfer required for prolonged corrosion and therefore improve the coating's

https://doi.org/10.1021/acsomega.2c05678
ACS Omega 2022, 7, 46717−46730

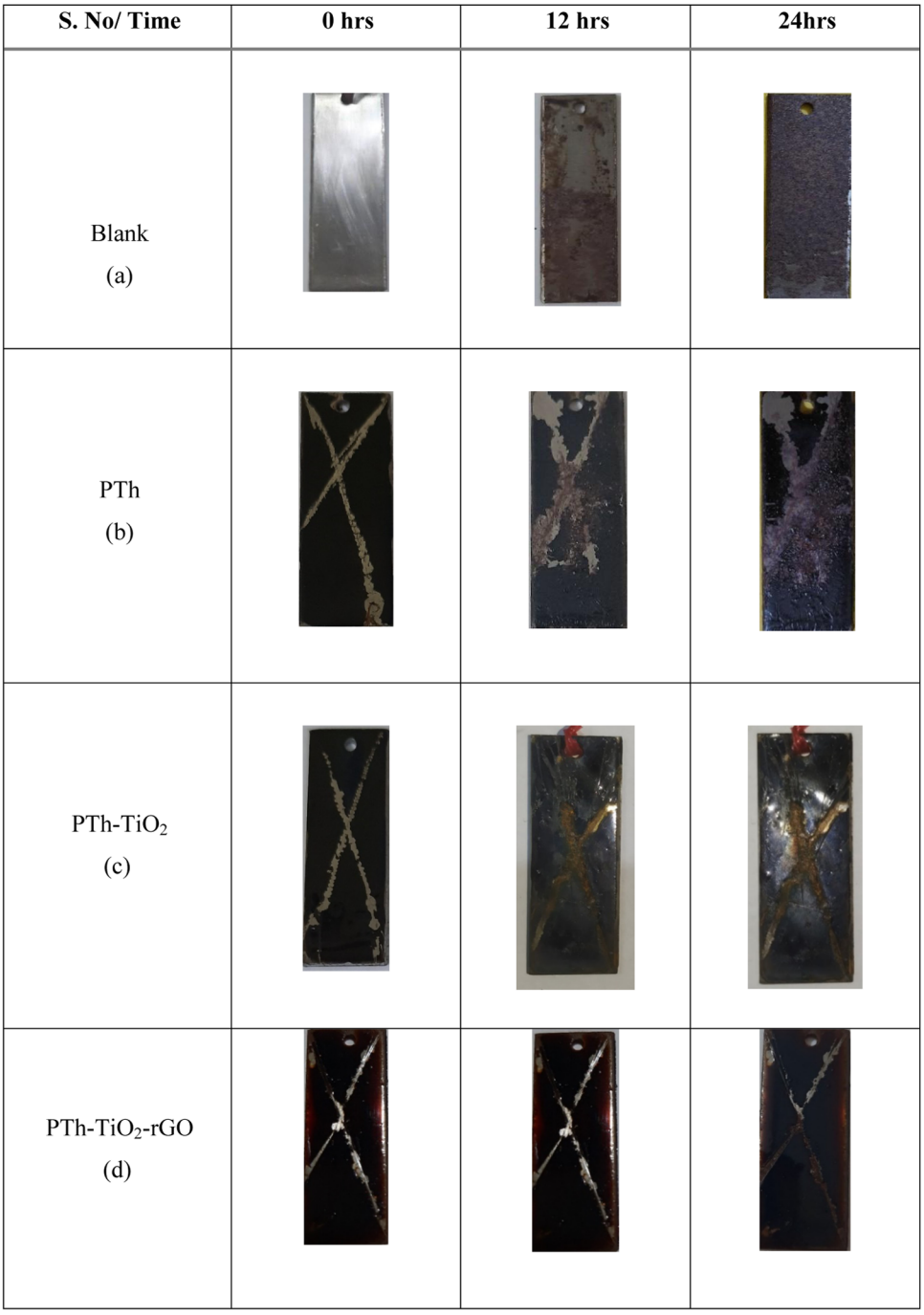

Figure 14. Digital images of coatings: (a) blank, (b) PTh, (c) PTh-TiO_2, and (d) PTh-TiO_2-rGO nanocomposite after salt spray test at various time durations.

corrosion protective efficiency.[42] The following mechanism can be used to explain the anticorrosion performance of incorporated rGO nanosheets in developed coatings. The addition of rGO to the electrolyte composition results in an increase in the oxide layer's thickness; thus, the tortuosity of the diffusion pathways for corrosive ions significantly increased, compared to the pure PTh and PTh-TiO_2 coatings. The PTh-TiO_2-rGO coating possesses the least pore density, in which rGO can act as a physical barrier to prevent the penetration of corroding substances to the coating/substrate interface due to its unique 2D structure and high specific surface area. The incorporation of rGO in the nanocomposite coating increases cross-sectional area resulting in the lower penetration of corrosive ions to the PTh-TiO_2-rGO nanocomposite coating. The absence of rGO in pure PTh and PTh-TiO_2 coatings lowers the barrier properties of the coatings and allows more penetration of corrosive ions in comparision to the PTh-TiO_2-rGO nanocomposite coating. Also, the presence of rGO in the nanocomposite coating results in a significant increase in contact angle indicating a decrease in the hydrophilic character of PTh-TiO_2-rGO coating.

https://doi.org/10.1021/acsomega.2c05678
ACS Omega 2022, 7, 46717−46730

Table 6. Chemical Constituents (wt %) of LCS

C	P	Mo	Mn	Cr	Al	V	Fe
0.049	0.028	0.081	0.723	0.051	0.01	0.033	balance

CONCLUSIONS

The PTh, PTh-TiO_2, and PTh-TiO_2-rGO nanocomposite were individually synthesized by chemical oxidative polymerization with $FeCl_3$ used as the oxidizing agent in the chloroform medium. In the PTh-TiO_2-rGO nanocomposite, the TiO_2 NPs and rGO were successfully incorporated. The FTIR spectra demonstrated the existence of strong interaction between rGO, PTh, and TiO_2 NPs. The addition of TiO_2 NPs has a significant impact on the crystalline nature of nanocomposites, as shown by the XRD patterns. The results of the salt spray and immersion test conducted on coated LCS suggest that the PTh-TiO_2-rGO nanocomposite coating provides significantly higher corrosion protection than PTh-TiO_2 and PTh coatings. The results of OCP measurements show much nobler potential for PTh-TiO_2-rGO nanocomposite-coated LCS coupons as compared to blank. Potentiodynamic polarization studies showed a noble shift (anodic shift) in E_{corr}, a substantial reduction in I_{corr}, and an increase in R_p values of the LCS steel in the presence of the PTh-TiO_2-rGO nanocomposite coating, and the EIS study demonstrated that PTh-TiO_2-rGO nanocomposite-coated LCS had the highest charge transfer resistance (R_{ct}) and the lowest coating capacitance (C_c). The overall studies suggest excellent corrosion protection behavior of the PTh-TiO_2-rGO nanocomposite coating on LCS in 3.5 wt % NaCl.

EXPERIMENTAL SECTION

Materials and Methods. Thiophene monomer (Merck), graphite powder (sigma), $FeCl_3$ (Merck), titanium(IV) isopropoxide (TTIP) (sigma), $CHCl_3$ (CDH), *N*-methyl-2-pyrrolidone (NMP) (Merck), BADGE epoxy resins (Sigma), triethylene tetraamine (Merck), HCl (analytical grade), NaCl (Merck), ethanol (analytical grade), and CTAB (CDH) were used as received. The LCS specimens (substrate) of the dimension 40.0 × 15.0 × 1.3 mm were used for salt spray tests and morphological examinations (immersion test), whereas circular specimens with a 1 cm^2 exposed surface area were used for electrochemical and wettability tests. The chemical composition (wt %) of LCS is given in Table 6. Before coating, the steel specimens were ground with different grit SiC sheets and then washed with acetone, followed by ethanol and double-distilled water, and finally dried in hot air.

Synthesis of TiO_2 Nanoparticles. We applied a blend of sol−gel and solvothermal techniques to make TiO_2 NPs, which was slightly modified from the procedure reported by Chen et al.[43,44] A typical TiO_2 NP synthesis involved dissolving 1 g of CTAB in 70 mL of ethanol, followed by the addition of 3 mg of potassium chloride (KCl). TTIP was incorporated into this solution at room temperature under harsh conditions. A milky white solution was obtained and stored for 24 h at room temperature, centrifuged, washed many times with ethyl alcohol, maintained at pH 10, and dried at room temperature. In addition, the synthesized sample was calcined at 100 °C. After that, the sample was dispersed in a 1:2 mixture of water and ethyl alcohol with an ammonia concentration of 0.2 M. The resultant mixture was then transferred to a hydrothermal autoclave and heated to 180 °C for 24 h. The resulting powder was dried at 450 °C for 3 h to eliminate the organic component, yielding TiO_2 NPs.[45]

Synthesis of rGO from Graphite Powder. rGO was synthesized by the oxidation of graphite powder according to the Hummers modified method, as described in our previous paper.[31]

Synthesis of PTh, PTh-TiO_2, and PTh-TiO_2-rGO Nanocomposite. We used an in situ chemical oxidative polymerization approach to make PTh, PTh-TiO_2, and PTh-TiO_2-rGO nanocomposite in chloroform, with anhydrous $FeCl_3$ as an oxidizing agent. For the preparation of PTh, 50 mL of chloroform was mixed with 5 mL of thiophene monomer and sonicated for 30 min to obtain a homogeneous solution (solution A). Further, 12.3 g of ferric chloride was dispersed in 100 mL of chloroform and stirred for 1 h to produce a homogeneous solution (solution B). Solution B was added dropwise into solution A with continuous stirring for 24 h. During the polymerization reaction, the room temperature was maintained throughout the reaction, and the color of the precipitated compound was changed from gray to brown; it was filtered, washed with ethanol, followed by double-distilled water, and kept in an oven at 60 °C for 24 h.

The PTh-TiO_2 nanocomposite was synthesized using an identical method. A specified amount (1 g) of synthesized TiO_2 nanoparticles was dispersed in 50 mL of chloroform and stirred for 30 min using ultrasonication at room temperature. The contents were transferred into a round-bottom flask, and 3 mL of thiophene was added to it and continuously stirred for 3 h. For the thiophene to adsorb onto the TiO_2 particles, the mixture was stirred for 30 min; this was followed by the addition of 50 mL of a saturated $FeCl_3$ solution. For 6 h, the reaction was carried out in an ice bath till the color of the precipitate changed from gray to black. The final product of PTh-TiO_2 was precipitated in ethanol, filtered through a Buchner funnel, and dried for 12 h at 60 °C in a vacuum oven.

For the preparation of the PTh-TiO_2-rGO nanocomposite, first, the TiO_2-rGO nanocomposite was synthesized. A homogeneous rGO suspension was prepared by dissolving 2 mg mL^{-1} rGO in 100 mL of aqueous ethanolic solution (1:1), followed by ultrasonication for 2 h. This was followed by the addition of 0.50 g of the synthesized TiO_2 NPs in this suspension, and the resultant suspension was agitated for 2 h. A brownish-black suspension with a pH of 10 was produced by the dropwise addition of a dilute NaOH solution to this suspension. The resultant TiO_2-rGO suspension was transferred into the autoclave at 180 °C for 24 h. After that, 0.5g of rGO-TiO_2 was dissolved in 50 mL of chloroform and sonicated for 1 h; this was followed by the addition of 3 mL of thiophene with continuous stirring for 30 min. Then, 8.3 g of ferric chloride was dispersed in 50 mL of chloroform and stirred for 1 h to make $FeCl_3$ solution. The $FeCl_3$ solution was added dropwise into the rGO-TiO_2 solution with continuous stirring for 24 h. The obtained precipitate of the PTh-TiO_2-rGO nanocomposite was centrifuged, washed, and dried at 60 °C in a vacuum oven for 12 h.

Characterization of the Synthesized Nanocomposites. *FTIR.* FTIR measurements were performed using a Perkin-Elmer FTIR spectrophotometer in the frequency limit

https://doi.org/10.1021/acsomega.2c05678
ACS Omega 2022, 7, 46717−46730

of 4000−400 cm^{-1} implementing the KBr disc technique on the synthesized nanocomposites PTh, PTh-TiO_2, and PTh-TiO_2-rGO.

XRD. XRD analyses were carried out on a Shimadzu 6100x X-ray diffractometer with Cu−K radiation and scanned in a 2θ range of 5−70°.

Raman Shift. Raman spectra of the materials were obtained using a confocal Raman microscope (Renishaw, UK) within a frequency range of 100−2000 cm^{-1}.

Surface Morphology. The materials' surface morphology was studied using SEM and TEM (Jeol JSM-6510LV and JEM-2100, respectively).

Corrosion Measurements. Anticorrosive performance of the uncoated and coated low-carbon steel in 3.5 wt % NaCl solution was investigated by OCP, PDP, and EIS measurements at room temperature using a potentiostat/galvanostat (model: 128N). The experiments were carried out in an Autolab ASTM corrosion cell (1 L) with uncoated and coated LCS samples with a 1 cm^2 exposed surface area as working electrodes, Ag/AgCl electrode (saturated KCl) as the reference electrode, and Pt wire as the counter electrode. The Tafel polarization was performed by sweeping the potential between ±250mV versus Ag/AgCl from OCP at a constant scan rate of 1.0 mV s^{-1}. EIS measurements were performed using a 10 mV perturbation at an open-circuit voltage and a frequency range of 10^{-2}−10^5 Hz.

Preparation of Coatings of PTh, PTh-TiO_2, and PTh-TiO_2-rGO Nanocomposite on LCS. The synthesized PTh-TiO_2-rGO, PTh-TiO_2, and PTh nanocomposites were individually cast on LCS coupons using NMP as solvent. First, 100 mg of coating materials were separately dissolved in 10 mL of NMP solvent; this was followed by the addition of 10 mg of epoxy resin with continuous stirring for 30 min and then polyamide curing agent (20 mg). The resultant solution was cast on LCS coupons. For complete elimination of the solvent, the coated samples were placed in a vacuum oven maintained at 50−60 °C for 5 h. The coating's thickness and uniformity were ensured by regularly monitoring the weight of the deposited polymer per unit surface area. The thickness of the coating was measured using an Elcometer (model: 456), and the coating thickness was found to be 14.9 ± 1 μm.

AUTHOR INFORMATION

Corresponding Author

Mohammad Mobin − *Corrosion Research Laboratory, Department of Applied Chemistry, Faculty of Engineering and Technology, Aligarh Muslim University, Aligarh 202002, India;* orcid.org/0000-0003-4829-7491; Phone: + 91-9411491161; Email: drmmobin@hotmail.com; Fax: + 91-571-2701895

Author

Farina Ansar − *Corrosion Research Laboratory, Department of Applied Chemistry, Faculty of Engineering and Technology, Aligarh Muslim University, Aligarh 202002, India*

Complete contact information is available at: https://pubs.acs.org/10.1021/acsomega.2c05678

Notes

The authors declare no competing financial interest.

ACKNOWLEDGMENTS

F.A., one of the authors, would like to thank UGC-Non-NET for their financial assistance. The authors are grateful to Aligarh Muslim University's USIF (University Sophisticated Instruments Facility) for providing access to their SEM, TEM, and Raman instruments.

REFERENCES

(1) Arthur, D- E.; Jonathan, A.; Ameh, P- O.; Anya, C. A review on the assessment of polymeric materials used as corrosion inhibitors of metals and alloys. *Int. J. Ind. Chem.* **2013**, *4*, 1−9.

(2) Münch, A. S.; Wolk, M.; Melanin, M.; Eichhorn, K.-J.; Simon, F.; Uhlmann, P. Smart functional polymer coatings for paper with antifouling properties. *J. Mater. Chem. B* **2018**, *6*, 830−843.

(3) Kamaraj, K.; Karpakam, V.; Azim, S. S.; Sathiyanarayanan, S. Electropolymerised polyaniline films as an effective replacement of carcinogenic chromate treatments for corrosion protection of aluminum alloys. *Synth. Met.* **2012**, *162*, 536−542.

(4) Grubač, Z.; Roncevic, I. S.; Metikos-Huković, M. Corrosion properties of the Mg alloy coated with polypyrrole films. *Corros. Sci.* **2016**, *102*, 310−316.

(5) Jadhav, N.; Kasisomayajula, S.; Gelling, V. Polypyrrole/Metal Oxides-Based Composites/Nanocomposites for Corrosion Protection. *Front. Mater.* **2020**, *7*, No. 95.

(6) Tallman, D. E.; Spinks, G.; Dominis, A.; Wallace, G. Electroactive conducting polymers for corrosion control. *J. Solid State Electrochem.* **2002**, *6*, 73−84.

(7) Breslin, C. B.; Fenelon, A- M.; Conroy, K- G. design, Surface engineering: corrosion protection using conducting polymers. *Mater. Des.* **2005**, *26*, 233−237.

(8) Hussein, M.; Al-Junaid, S. S.; Abu-Zied, B- M.; Hermas, A.-E. Electrodeposition and corrosion protection performance of polypyrrole composites on aluminum. *Int. J. Electrochem. Sci.* **2016**, *11*, 3938−3951.

(9) Bedre, M- D.; Deshpande, R.; Salimath, B.; Abbaraju, V. Preparation, and characterization of polyaniline-Co3O4 nanocomposites via interfacial polymerization. *Am. J. Mater. Sci.* **2012**, *2*, 39−43.

(10) Wang, S.; Tan, Z.; Li, Y.; Sun, L.; Li, Y. kinetic analysis of thermal decomposition of polyaniline/ZrO 2 Composite. *J. Therm. Anal. Calorim.* **2008**, *92*, 483−487.

(11) Wilke, B. M.; Zhang, L. Electrochemical investigations of polycaprolactone-coated AZ31 Mg alloy in Earle's balanced salt solution and conventional simulated body fluid. *JOM* **2016**, *68*, 1701−1710.

(12) Lyon, S. B.; Bingham, R.; Mills, D. Advances in corrosion protection by organic coatings: What we know and what we would like to know. *Prog. Org. Coat.* **2017**, *102*, 2−7.

(13) Xavier, J. R. Experimental investigation of the hybrid epoxy-silane coating for enhanced protection against the corrosion of aluminum alloy AA7075 frame in solar cells. *Macromol. Res.* **2020**, *28*, 501−509.

(14) Dalmoro, V.; dos Santos, J. H.; Armelin, E.; Alemán, C.; Azambuja, D- S. synergistic combination of tetraethylorthosilicate and multiphosphonic acid offers excellent corrosion protection to AA1100 aluminum alloy. *Appl. Surf. Sci.* **2013**, *273*, 758−768.

(15) Kausar, A. Characterization, Polyimide, polybenzimidazole-in situ-polyaniline nanoparticle and carbon nano-onion-based nanocomposite designed for corrosion protection. *Int. J. Polym. Anal.* **2017**, *22*, 557−567.

(16) Caldona, E. B.; Albayalde, J.; Aglosolos, A. M. P.; Bautista, K. S.; Tavora, M. D.; Cabalza, S. A. P.; Diaz, J. R- O.; Mulato, M- D. Environment, Titania-containing recycled polypropylene surfaces with photo-induced reversible switching wettability. *J. Polym. Environ.* **2019**, *27*, 1564−1571.

(17) Cui, X.; Zhu, G.; Pan, Y.; Shao, Q.; Zhao, C. x.; Dong, M.; Dong, M.; Zhang, Y.; Zhang, Y.; Guo, Z. Polydimethylsiloxane-titania nanocomposite coating: fabrication and corrosion resistance. *Polymer* **2018**, *138*, 203−210.

https://doi.org/10.1021/acsomega.2c05678
ACS Omega 2022, 7, 46717−46730

(18) Chao, D.; Ma, X.; Lu, X.; Cui, L.; Mao, H.; Zhang, W.; Wei, Y. J. Electroactive hyperbranched polyamide synthesized by oxidative coupling polymerization within an A2+ B3 Strategy. *Macromol. Chem. Phys.* **2007**, *208*, 658−664.
(19) Kirkland, N.; Schiller, T.; Medhekar, N.; Birbilis, N. Exploring graphene as a corrosion protection barrier. *Corros. Sci.* **2012**, *56*, 1−4.
(20) Sun, W.; Wang, L.; Wu, T.; Pan, Y.; Liu, G. Synthesis of low-electrical-conductivity graphene/pernigraniline composites and their application in corrosion protection. *Carbon* **2014**, *79*, 605−614.
(21) Wu, Z.-S.; Ren, W.; Gao, L.; Zhao, J.; Chen, Z.; Liu, B.; Tang, D.; Yu, B.; Jiang, C.; Cheng, H.-M. Synthesis of graphene sheets with high electrical conductivity and good thermal stability by hydrogen arc discharge exfoliation. *ACS Nano* **2009**, *3*, 411−417.
(22) Berry, V. Impermeability of graphene and its applications. *Carbon* **2013**, *62*, 1−10.
(23) Kim, K. S.; Zhao, Y.; Jang, H.; Lee, S. Y.; Kim, J. M.; Kim, K. S.; Ahn, J.-H.; Kim, P.; Choi, J.-Y.; Hong, B.-H. Large-scale pattern growth of graphene films for stretchable transparent electrodes. *Nature* **2009**, *457*, 706−710.
(24) Husain, A.; Ahmad, S.; Mohammad, F. Synthesis, characterization and ethanol sensing application of polythiophene/graphene nanocomposite. *Mater. Chem. Phys.* **2020**, *239*, 122324.
(25) Gök, A.; Omastova, M.; Yavuz, A. Synthesis, and characterization of polythiophenes prepared in the presence of surfactants. *Synth. Met.* **2007**, *157*, 23−29.
(26) Karim, M. R.; Lee, C. J.; Lee, M. Synthesis and characterization of conducting polythiophene/carbon nanotubes composites. *J. Polym. Sci., Part A: Polym. Chem.* **2006**, *44*, 5283−5290.
(27) Yu, Z.; Di, H.; Ma, Y.; He, Y.; Liang, L.; Lv, L.; Ran, X.; Pan, Y.; Luo, Z. Preparation of graphene oxide modified by titanium dioxide to enhance the anti-corrosion performance of epoxy coatings. *Surf. Coat. Technol.* **2015**, *276*, 471−478.
(28) Shi, G.; Xu, J.; Fu, M. Raman spectroscopic and electrochemical studies on the doping level changes of polythiophene films during their electrochemical growth processes. *J. Phys. Chem. B* **2002**, *106*, 288−292.
(29) Alam, R.; Mobin, M.; Aslam, J. Polypyrrole/graphene nanosheets/rare earth ions/dodecyl benzene sulfonic acid nanocomposite as a highly effective anticorrosive coating. *Surf. Coat. Technol.* **2016**, *307*, 382−391.
(30) Saravanan, K.; Sathiyanarayanan, S.; Muralidharan, S.; Azim, S. S.; Venkatachari, G. Performance evaluation of polyaniline pigmented epoxy coating for corrosion protection of steel in a concrete environment. *Prog. Org. Coat.* **2007**, *59*, 160−167.
(31) Mobin, M.; Ansar, F.; Shoeb, M.; Parveen, M.; Aslam, J. Synergistic effect of graphene polyindole nanocomposite for enhanced corrosion protection of aqueous coating in 3.5% NaCl solution for low carbon steel. *Nanoselect* **2021**, *2*, 293−302.
(32) Vera, R.; Schrebler, R.; Cury, P.; Del Rio, R.; Romero, H. Corrosion protection of carbon steel and copper by polyaniline and poly (ortho-methoxyaniline) films in sodium chloride medium. An electrochemical and morphological study. *J. Appl. Electrochem.* **2007**, *37*, 519−525.
(33) Mansfeld, F. Recording and analysis of AC impedance data for corrosion studies. *Corrosion* **1981**, *37*, 301−307.
(34) Hsu, C.; Mansfeld, F. Concerning the conversion of the constant phase element parameter Y0 into a capacitance. *Corrosion* **2001**, *57*, 9.
(35) Grgur, B. N.; Zivkovic, P.; Gvozdenovic, M. Kinetics of the mild steel corrosion protection by polypyrrole-oxalate coating in sulfuric acid solution. *Prog. Org. Coat.* **2006**, *56*, 240−247.
(36) Bisht, B.; Bhandari, H.; Ruhi, G.; Gairola, S.; Dhawan, S- K. Evaluation of an advanced self-healing and highly durable corrosion protective epoxy coating modified with poly (Aniline-co-Pentafluoroaniline)/ZrO2 nanocomposite on mild steel. *Curr. Smart Mater.* **2017**, *2*, 130−145.
(37) Madhan Kumar, A.; Gasem, Z- M. In situ electrochemical synthesis of polyaniline/f-MWCNT nanocomposite coatings on mild steel for corrosion protection in 3.5% NaCl solution. *Prog. Org. Coat.* **2015**, *78*, 387−394.
(38) Chen, Z.; Yang, W.; Yin, X.; Chen, Y.; Liu, Y.; Xu, B. Corrosion protection of 304 stainless steel from a smart conducting polypyrrole coating doped with pH-sensitive molybdate-loaded TiO2 nano containers. *Prog. Org. Coat,* **2020**, *146*, 105750.
(39) Chang, C.-H.; Huang, T.-C.; Peng, C.-W.; Yeh, T.-C.; Lu, H.-I.; Hung, W.-I.; Weng, C.-J.; Yang, T.-I.; Yeh. Novel anticorrosion coatings prepared from polyaniline/graphene composites. *Carbon* **2012**, *50*, 5044−5051.
(40) Beikmohammadi, M.; Fotouhi, L.; Ehsani, A.; Naseri, M. Potentiodynamic and electrochemical impedance spectroscopy study of anticorrosive properties of p-type conductive polymer/TiO2 nanoparticles. *Solid State Ionics* **2018**, *324*, 138−143.
(41) Hosseini, M.; Fotouhi, L.; Ehsani, A.; Naseri, M. Enhancement of corrosion resistance of polypyrrole using metal oxide nanoparticles: Potentiodynamic and electrochemical impedance spectroscopy study. *J. Colloid Interface Sci.* **2017**, *505*, 213−219.
(42) Wessling, B. Passivation of metals by coating with polyaniline: corrosion potential shift and morphological changes. *Adv. Mater.* **1994**, *6*, 226−228.
(43) Chen, D.; Cao, L.; Huang, F.; Imperia, P.; Cheng, Y.-B.; Caruso, R.-A. Synthesis of monodisperse mesoporous titania beads with controllable diameter, high surface areas, and variable pore diameters (14−23 nm). *J. Am. Chem. Soc.* **2010**, *132*, 4438−4444.
(44) Chen, D.; Huang, F.; Cheng, Y. B.; Caruso, R.-A. Mesoporous anatase TiO2 beads with high surface areas and controllable pore sizes: a superior candidate for high-performance dye-sensitized solar cells. *Adv. Mater.* **2009**, *21*, 2206−2210.
(45) Shoeb, M.; Mobin, M.; Ali, A.; Zaman, S.; Naqvi, A. H. Graphene-mesoporous anatase TiO2 nanocomposite: A highly efficient and recyclable heterogeneous catalyst for the one-pot multicomponent synthesis of benzodiazepine derivatives. *Appl. Organomet. Chem.* **2018**, *32*, e3961.

https://doi.org/10.1021/acsomega.2c05678
ACS Omega 2022, 7, 46717−46730